Supplement of Ocean Sci., 22, 167–185, 2026
https://doi.org/10.5194/os-22-167-2026-supplement

Ocean Science Open Access EGU

Supplement of

A decade of continuous Rockall Trough transport observations using moorings and gliders

Kristin Burmeister et al.

Correspondence to: Kristin Burmeister (kristin.burmeister@sams.ac.uk)

S1 Data loss and gap filling of moored observations

The data return of the moored hydrographic and velocity instruments are generally very high. However, a few data gaps occurred due to battery failure or instrument loss and the different gap filling methods are described below.

At EB1, a data gap in the hydrographic observations (Figure 2 c,e) due to battery failure and fishing damage of the upper two Conductivity-Temperature-Depth sensors (CTDs) between March and May 2017 is filled using linear regressions with the time series at WB1 (Houpert et al., 2020).

No velocity observations are available between April 2016 and beginning of July 2016 due to the wrong type of battery installed on the deployed current meters (Figure 2a,b). Due to the high correlation between adjacent instruments at one mooring, the longest velocity record of each mooring is used to extent the records of the other instruments before the data is gridded on a regular depth grid. Therefore, we normalise the longest velocity record by its mean and standard deviation and then scale the normalised time series to have the same mean and standard deviation as the instrument record at the target depth for that deployment period. The instrument records are consecutively filled starting with the instruments closest to the one with the longest record. A three months data gap remains where no velocity data is available. For the Rockall Trough transport calculation, the three months gap in the gridded velocity data is filled by temporal linear interpolation (Houpert et al., 2020; Fraser et al., 2022).

At the end of the 2016-2017 mooring deployment the upper two current meters at EB1 malfunctioned and suspicious data are removed between end of March and beginning of May 2017 (Figure 2a). Similar to the previous deployment, we normalise velocities observed from the next closest instrument at 500 m depth and fill the data gaps in the upper two instrument records by scaling the normalised time series of the 500 m instrument with the mean and standard deviation of the instruments at the target depth for the same deployment period.

During the deployment period from October 2020 to July 2022 the deepest current meter at EB1 was flooded with seawater hence no velocity data is available at 1780 m (Figure 2a). To reconstruct the time series of the deepest instrument we normalise the velocity observations from the nearest instrument at 1350 m by the mean and standard deviation including the previous deployment period (July 2018 to July 2022) and scaled the normalised time series with the mean and standard deviation derived from the instrument at 1780 m using the previous deployment period (July 2018 to October 2020).

S2 Along-isobath transformation of glider transects

To enable computation of means and composites from glider transects that follow slightly different paths, all transects are mapped onto a common zonal subsection of the eastern wedge (Figure S1). This subsection spans from mooring EB1 (9.6°W) to 9.2°W along 57.1°N. The approach assumes that ESC streamlines follow isobaths and that tracers are conserved along isobaths within the glider survey region. The methodology for this transformation is outlined below, with a more detailed description provided in Fraser et al. (2022).

The eastern wedge subsection has a horizontal coordinate x and a vertical coordinate z. Because the bathymetry H varies monotonically with x, we may express it as a function $H = f(x)$ with inverse $x = f^{-1}(H)$. For any given glider track, we

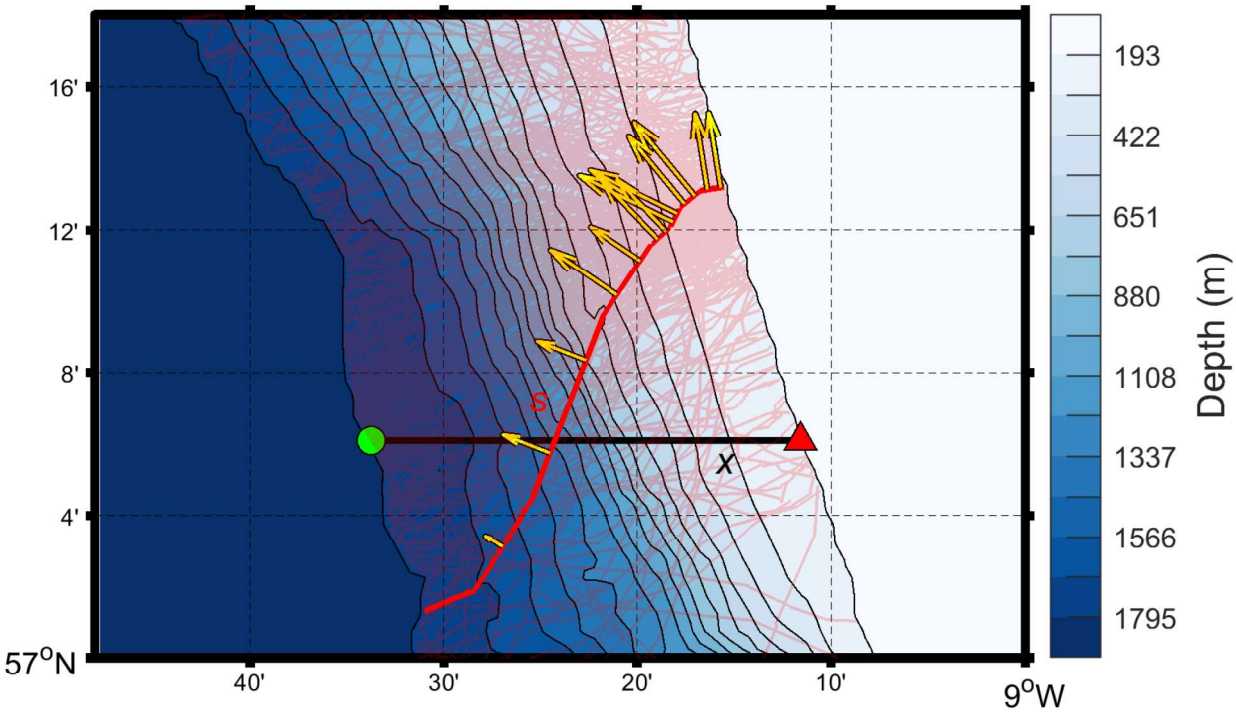

Figure S1. Along-isobath projection of glider transects in the eastern wedge of the Rockall Trough. Bathymetry is shown in color shading. Individual glider transects across the slope are indicated by faint red lines and parameterised by along-path horizontal coordinate s. The bold black line, labeled x, represents the eastern wedge subsection between the EB1 mooring (green circle) and the section endpoint (red triangle). One arbitrary glider transect is highlighted in bold red as an example, with yellow arrows showing the cross-sectional component of the depth-averaged velocity.

introduce the along-path horizontal coordinate s and evaluate $H(s)$ at each location (Figure S1). An associated x-coordinate is then assigned to each point s via the mapping:

$$x \equiv f^{-1}(H(s)). \tag{S1}$$

Note that $H(s)$ does not need to be monotonic. This mapping is conceptually equivalent to projecting each point on the glider path s onto the eastern wedge subsection x by sliding it along isobaths (Figure S1). Scalar hydrographic variables are then transferred to the section using the relation:

$$\Theta(s,z) \rightarrow \Theta(x,z) \tag{S2}$$

$$S(s,z) \rightarrow S(x,z) \tag{S3}$$

To evaluate the volume transport across a given glider transect, we first compute the component of depth-averaged current locally perpendicular to the path s. When mapped from s-space to x-space, this corresponds to a meridional velocity component, $\overline{m}$, at each horizontal position x. Conservation of transport under this transformation requires a local scaling by $\frac{\partial s}{\partial x}$, yielding the depth-averaged meridional velocity:

$$\overline{v}(x) = \overline{m}(x)\frac{\partial s}{\partial x}. \tag{S4}$$

This procedure guarantees that the computed volume transport, Q, between any pair of isobaths is preserved. In the uncommon cases where the glider trajectory becomes nearly aligned with the isobaths, the factor $\frac{\partial s}{\partial x}$ tends toward $\pm\infty$. To avoid unphysical amplification, we constrain this term to the range $-4 \leq \frac{\partial s}{\partial x} \leq 4$, clipping any values outside these bounds. Although this truncation introduces a small error in the transformed velocity field, the excluded component corresponds to flow nearly perpendicular to the isobaths and therefore lies outside the focus of this analysis.

The transformed Θ and S points are then interpolated onto the eastern wedge subsection grid, which using horizontal and vertical resolutions of $dx \approx 250,\mathrm{m}$ and $dz = 10,\mathrm{m}$, using a Barnes (1994) interpolation with smoothing length scales of $3,\mathrm{km}$ and $10,\mathrm{m}$. We then calculate potential density, $\sigma_0(x,z)$, from the resulting fields. The transformed depth-averaged meridional velocities, $\overline{v}(x)$, are similarly interpolated with the Barnes (1994) method, but applied only in the horizontal (x) direction.

In order to study the two-dimensional velocity structure on our common zonal section, we add the vertical shear computed from the thermal wind relation, ensuring that the added shear term vanishes upon depth integration, i.e.:

$$v(x,z) = v_0(x,z) - \frac{1}{H}\int_{-H}^{0} v_0(x,z)dz + \overline{v}(x) \tag{S5}$$

S3 Supplementary tables

Table S1. Comparison of heat (Q_h) and freshwater (Q_f) transports estimated from full temperature–salinity sections versus profiles at mooring positions. "Mean full" and "Std Dev full" represent the mean and 1 standard deviation calculated from complete ship sections (western wedge, mid-basin) or full glider sections (upper 1000m, eastern wedge). "Mean profile" and "Std Dev profile" represent calculations using data only at WB1/2 and EB1 positions from ship sections (western wedge, mid-basin) or glider data (upper 1000 m, eastern wedge). Mean bias error and root-mean-square error (RMSE) between full-section and profile-based heat and freshwater transports are also shown. Only ship sections covering all Extended Ellet Array stations in the western wedge or the mid basin, respectively, were used. Units are 10^{-2} Sv for freshwater transport and 10^{-2} PW for heat transport.

	Western wedge 10 ship sections		**Mid basin** 8 ship sections		**Eastern wedge** 166 glider sections	
	Qf (10^{-2} Sv)	Qh (10^{-2} PW)	Qf (10^{-2} Sv)	Qh (10^{-2} PW)	Qf (10^{-2} Sv)	Qh (10^{-2} PW)
Mean full	0.2318	-0.4271	-2.7922	6.2001	-0.4302	1.1905
Mean profile	0.2375	-0.4243	-3.6571	7.5898	-0.4352	1.1165
Mean bias error	-0.0057	-0.0028	0.8649	-1.3896	0.0050	0.0740
Std Dev full	1.5705	3.3299	5.6241	11.0403	0.6610	1.6653
Std Dev profile	1.6191	3.4229	5.1163	10.1347	0.6719	1.5980
RMSE	0.0819	0.1212	1.4615	2.8992	0.1240	0.1389

Table S2. 10 year trends and p-value (Hamed and Rao, 1998) for volume (Q), heat (Q_h) and freshwater (Q_f) transports. Trends significant on a 5% significant level are shown as bold.

	Western wedge		**Mid basin**		**Eastern wedge**	
	Trend	P-value	Trend	P-value	Trend	P-value
Q (Sv)	**1.66**	**0.00**	**-2.24**	**0.00**	-0.37	0.48
Q_h (10^{-2} PW)	**0.77**	**0.000**	**-1.04**	**0.048**	-0.16	0.703
Q_f (10^{-2} Sv)	**-0.48**	**0.000**	0.82	0.100	0.12	0.591

Table S3. Pearson correlation coefficient (R), p-value (p), and explained variance (R^2) for the relationship between heat (Q_h) and freshwater (Q_f) transports and depth integrated conservative temperature (T) and absolute salinity (S) profiles at WB1/2 (western wedge), the average of WB1/2 and EB1 (mid basin), and EB1 (eastern wedge).

Region	Q_h **vs** T	Q_f **vs** S
Total		
Pearson R	0.19	-0.47
P-value (p)	0.00	0.00
R^2	4%	22%
Western wedge		
Pearson R	0.46	0.06
P-value (p)	0.00	0.00
R^2	21%	0%
Mid basin		
Pearson R	0.17	-0.47
P-value (p)	0.00	0.00
R^2	3%	22%
Eastern wedge		
Pearson R	-0.16	-0.33
P-value (p)	0.00	0.00
R^2	3%	11%

S4 Supplementary figures

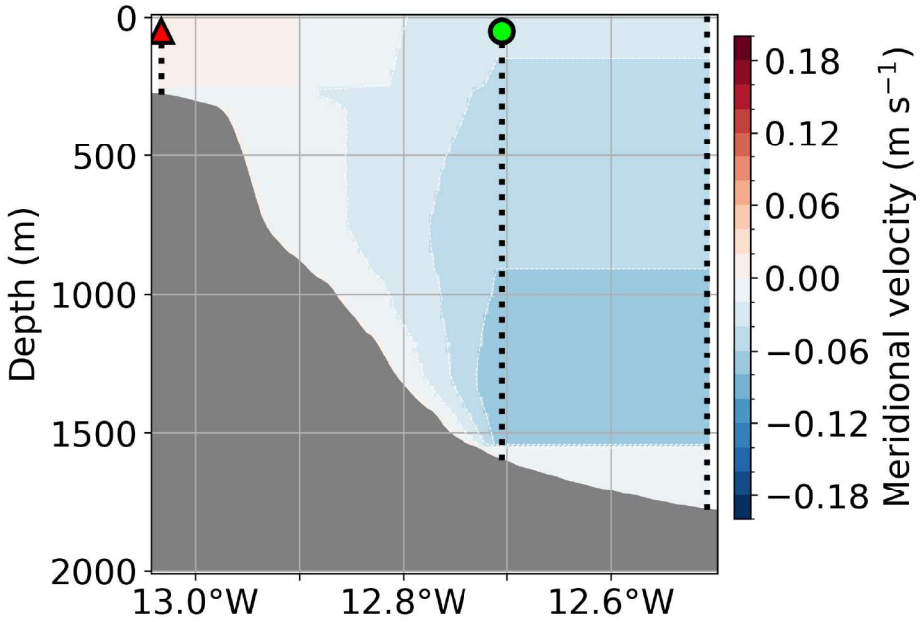

Figure S2. Averaged meridional velocity for the western wedge. From left to right: black dotted line with red triangle marks the western limit of the section, black dotted line with green circle marks mooring WB1, black dotted line without marker marks WB1/2 which is the eastern limit of the section.

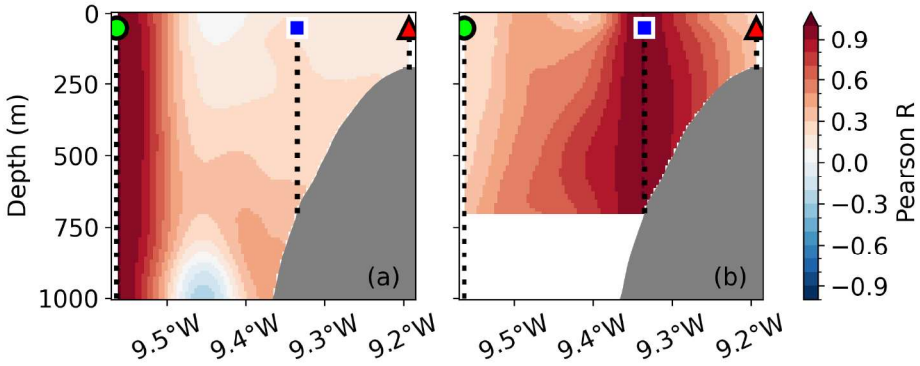

Figure S3. Correlation sections of sub-sampled glider velocity profiles at (a) EB1 and (b) RTADCP with velocities across the full glider section. Black dotted line with green circle marks mooring EB1, black dotted line with blue square marks the position of the RTADCP, black dotted line with red triangle marks the eastern limit of the section.

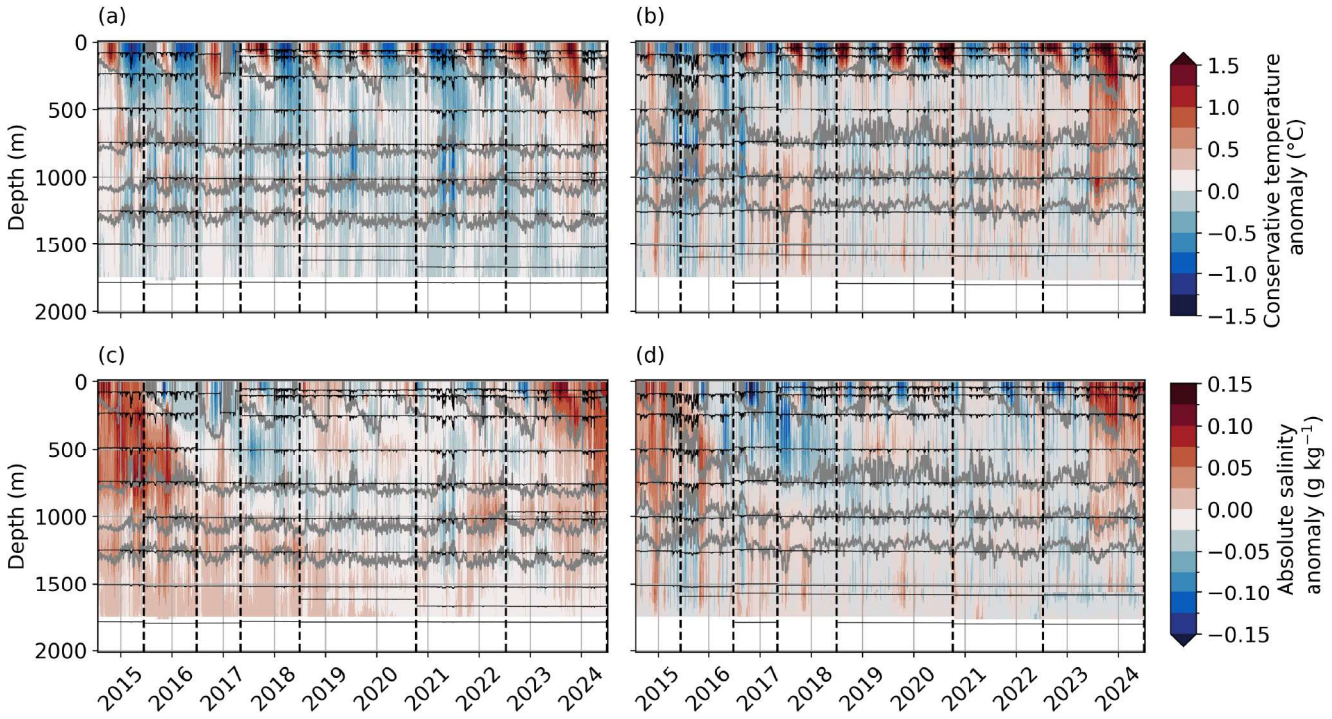

Figure S4. Temporal temperature (a,b) and salinity (c,d) anomalies, relative to the 2014–2024 mean from the EB1 (a,c) and WB1/2 (b,d) moorings. Black lines mark the pressure time series for the single CTD sensors. Grey contour lines show potential density values at 27.2, 27.4, 27.6 and 27.7 kg m^{-3} (top to bottom). Vertical dashed black line indicate the individual servicing cruises for the moorings.

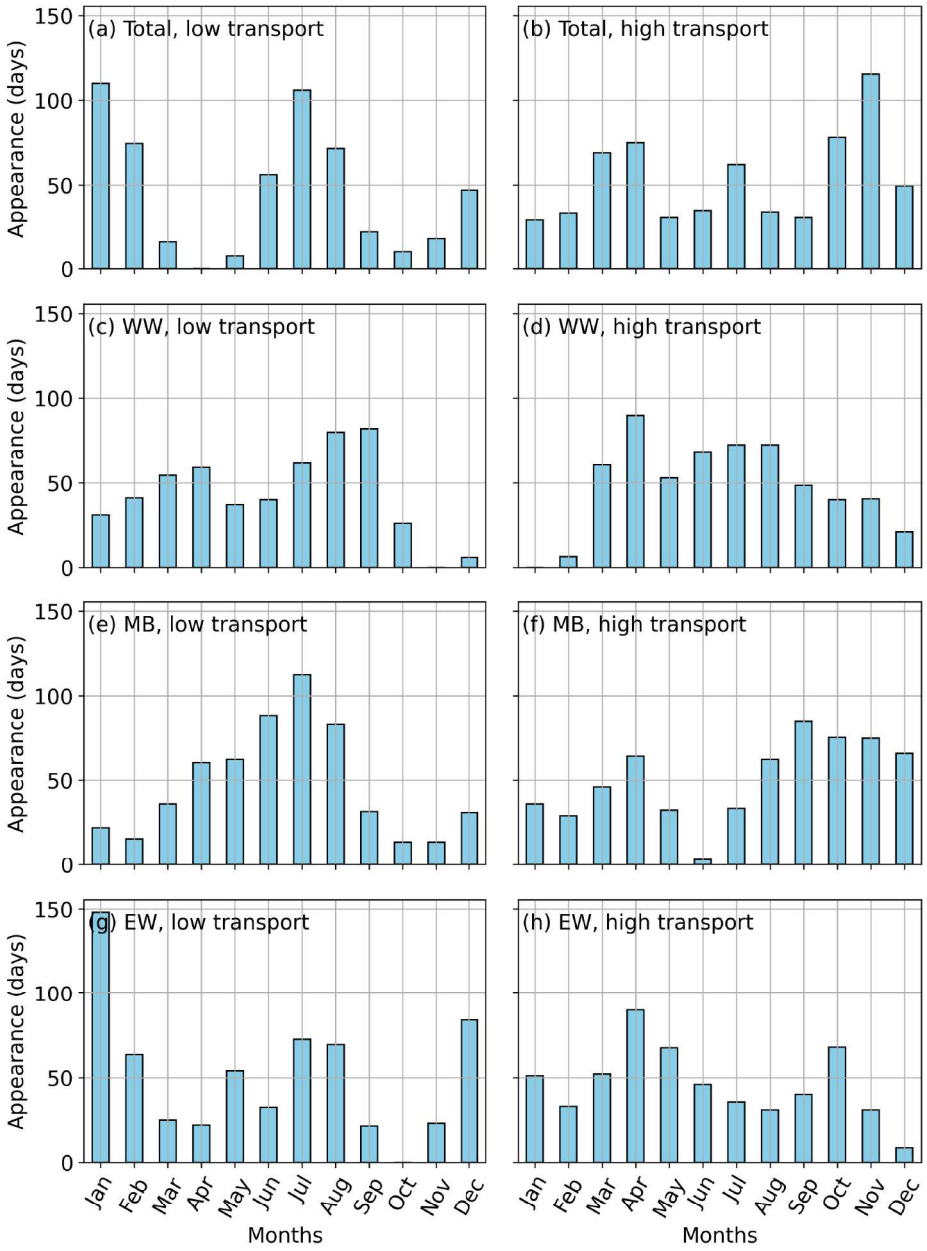

Figure S5. Seasonality of extreme transport events in the Rockall Trough for the full (total), western wedge (WW), mid basin (MB) and eastern wedge (EW) section. Total number of days per month when the 90-day low-pass filtered time series (a,c,e,g) is lower than mean - 1 standard deviation and (b,d,f,h) exceeds mean + 1 standard deviation.

References

Barnes, S. L.: Applications of the Barnes Objective Analysis Scheme. Part II: Improving Derivative Estimates, Journal of Atmospheric and Oceanic Technology, 11, 1449–1458, https://doi.org/10.1175/1520-0426(1994)011<1449:AOTBOA>2.0.CO;2, 1994.

Fraser, N. J., Cunningham, S. A., Drysdale, L. A., Inall, M. E., Johnson, C., Jones, S. C., Burmeister, K., Fox, A. D., Dumont, E., Porter, M., and Holliday, N. P.: North Atlantic Current and European Slope Current Circulation in the Rockall Trough Observed Using Moorings and Gliders, Journal of Geophysical Research: Oceans, 127, https://doi.org/10.1029/2022JC019291, 2022.

Hamed, K. H. and Rao, A. R.: A modified Mann-Kendall trend test for autocorrelated data, Journal of Hydrology, 204, 182–196, https://doi.org/10.1016/S0022-1694(97)00125-X, 1998.

Houpert, L., Cunningham, S., Fraser, N., Johnson, C., Holliday, N. P., Jones, S., Moat, B., and Rayner, D.: Observed Variability of the North Atlantic Current in the Rockall Trough From 4 Years of Mooring Measurements, Journal of Geophysical Research: Oceans, 125, 1–9, https://doi.org/10.1029/2020JC016403, 2020.